International Journal for Numerical and Analytical Methods in Geomechanics

WILEY

RESEARCH ARTICLE OPEN ACCESS

Bayesian Neural Network Prediction and Uncertainty Analysis of Bio-Cemented Soil Strength

Aoxi Zhang[1,2] | Liang Wang[3] | Wengang Zhang[4] | Chaofa Zhao[1] | Pan Zhang[5]

[1]Department of Civil Engineering, Computing Center for Geotechnical Engineering, Zhejiang University, Hangzhou, China | [2]Urban and Environmental Engineering Research Unit, University of Liège, Liège, Belgium | [3]Department of Geoscience & Engineering, Delft University of Technology, Delft, the Netherlands | [4]School of Civil Engineering, Chongqing University, Chongqing, China | [5]Department of Civil Engineering, University of Ottawa, Ottawa, Canada

Correspondence: Liang Wang (l.wang-10@tudelft.nl)

Received: 15 May 2025 | **Revised:** 28 October 2025 | **Accepted:** 12 November 2025

Keywords: Bayesian neural network | bio-cemented soils | microbially induced calcite precipitation | probabilistic modelling | strength prediction | uncertainty quantification

ABSTRACT

Microbially induced carbonate precipitation (MICP) has emerged as a promising ground improvement technique, with MICP-treated soils exhibiting substantial enhancements in strength. However, experimental results revealed significant variability in strength outcomes of MICP-treated soils, even under identical treatment conditions and soil properties. This uncertainty in strength is challenging to capture using traditional predictive approaches such as conventional constitutive models. The present study leverages artificial intelligence to address the challenge by developing a Bayesian neural network (BNN) model for predicting the strength of bio-cemented soils while considering uncertainty. A dataset comprising 480 experimental samples was used to develop the model. The results indicate that carbonate content and confining pressure emerge as the most influential factors governing the strength of bio-cemented soils. The BNN model exhibits lower uncertainty when predicting bio-cemented soils with relatively low strength, while demonstrating higher uncertainty for soils with strength exceeding 2 MPa. Moreover, micromechanical investigations using the discrete element method (DEM) reveal that multiscale factors, including crystal distribution patterns, fabric and spatial heterogeneity of precipitates, contribute significantly to the strength uncertainty of bio-cemented soils. The developed BNN model provides an alternative tool for predicting bio-cemented soil strength with quantified reliability, facilitating the design of MICP treatment and its application in geotechnical engineering.

1 | Introduction

To reinforce soils with poor mechanical properties, ground improvement is essential. Soil bio-cementation via microbially induced carbonate precipitation (MICP) has emerged as a promising solution for soil improvement. This method harnesses the metabolic activities of microorganisms to precipitate calcium carbonate within soil matrices, thereby improving soil strength. In this biochemical process, urea, calcium chloride and bacterial solution are needed as input solutions. The ureolytic bacteria, such as *Sporosarcina pasteurii*, catalyse the hydrolysis of urea into ammonium and carbonate ions. This leads to the precipitation of calcium carbonate crystals in the presence of calcium ions. Compared to the conventional ground improvement methods, such as deep mixing and dynamic compaction, the MICP method demonstrates several advantages, such as consuming less energy [1] and causing less disturbance to the surrounding infrastructures during the treatment [2]. Consequently, MICP has been applied in various geotechnical engineering applications, including foundation stabilisation, slope reinforcement, liquefac-

tion mitigation, reinforcement of rock discontinuity [3–5], and erosion control.

The mechanical strength of bio-cemented soils is a critical parameter for assessing the effectiveness of MICP treatment. Establishing a model to predict the strength of bio-cemented soil is important for its potential applications in geotechnical engineering. On the one hand, for a given treatment program (e.g., the concentration of urea and calcium chloride solution), the resulting strength can be estimated through a well-established predicting model. On the other hand, for a target strength to be achieved through MICP, the predicting model can be utilised to fine-tune the treatment program.

In general, strength prediction for MICP-treated soils often considers only a limited number of variables, such as calcite content. For instance, Cheng et al. [6] established empirical correlations linking the unconfined compressive strength to calcite content. Gai and Sanchez [7] built a constitutive model in which calcite content is used as the parameter describing mechanical improvement. While these approaches provide a valuable foundation for prediction, they fail to capture the full complexity of the multi-physical bio-cementation process and its impact on soil strength. Accurately predicting the strength of MICP-treated soils remains challenging due to the complex interplay of various factors influencing the bio-cementation process. A detailed review of the influencing factors is presented in Section 2.

Recent advancements in machine learning (ML) techniques have opened new avenues for developing more sophisticated models for predicting soil properties. These sophisticated models demonstrate the powerful predictive capabilities of ML methods. To date, only a few studies have been conducted to predict the strength of bio-cemented soils using machine learning. Wang and Yin [8] used multi-expression programming (MEP) combined with the Monte-Carlo (MC) method to predict the unconfined compressive strength (UCS) of MICP-treated sands. Following that, Nawaz et al. [9] compared different ML methods, including Gaussian Process Regression (GPR), Adaptive Neuro Fuzzy Inference System (ANFIS), Artificial Neural Network (ANN), and Gene Expression Programming (GEP) in the performance of predicting UCS of MICP-treated soils. Sangdeh et al. [10] used ANN and ANFIS to predict both the carbonate content and UCS of MICP-treated sands. Their ML models provide alternatives to constitutive models for predicting the strength of bio-cemented soils. Despite these advancements, current ML approaches for predicting bio-cemented soil strength face several limitations. Existing studies predominantly focused on predicting the unconfined compressive strength, neglecting confined conditions, that are crucial and commonly encountered in practical scenarios. This limits the practical applicability of these models since most soils experience complex stress states involving confinements. Moreover, conventional ANNs provide deterministic predictions without quantifying the uncertainties. However, this uncertainty quantification is particularly crucial for MICP-treated soils, as it was found that soil with identical physical properties (e.g., D_{50}, particle size distribution and e_0) subjected to the same treatment program can exhibit substantially different strength improvements [11, 12]. Such variability suggests the necessity of incorporating uncertainty quantification into predictive models for bio-cemented soil strength. Consequently, there exists a significant research gap in developing a predictive model that can simultaneously predict confined strength and quantify associated uncertainties for MICP-treated soils.

Bayesian Neural Networks (BNNs) offer a compelling solution to address this limitation. Unlike traditional neural networks that provide deterministic estimates, BNNs adopt a probabilistic approach by treating model parameters as probability distributions rather than fixed values, allowing for providing not only predictions but also associated confidence intervals. Consequently, Bayesian theory and BNN have been widely applied in geotechnical applications [13–16]. Furthermore, BNNs incorporate prior knowledge into the model and are less prone to overfitting, making them particularly suitable for the relatively small datasets often available in bio-cementation research.

To this end, this study aims to develop a BNN model to predict the strength of MICP-treated soils, with the following advancements beyond current research:

1. A more comprehensive dataset has been constructed by enriching the dataset from Wang and Yin [8] by 37% with newly published data.
2. The confining pressure is taken into consideration, and hence the model established in this study is able to predict the strength of bio-cemented soil under confining stress.
3. BNN is employed to take into consideration the prediction uncertainty.
4. A detailed discussion combined with discrete element method (DEM) simulations is provided to understand the potential physical mechanisms leading to the strength uncertainty.

This study is organised as follows: Section 2 reviews the factors influencing the mechanical properties of bio-cemented soils; Section 3 introduces the database and methods used in this study; Section 4 presents the performance of the ANN and BNN models; Section 5 discusses the potential physical mechanisms underlying the uncertainty; and Section 6 summarises the main conclusions of this study and provides recommendations for future research.

2 | Factors Affecting Bio-Cemented Soil Strength

To develop a neural network model for predicting the strength of bio-cemented soils, it is crucial to first identify the potential factors influencing soil strength. This section provides a concise overview of how various factors affect soil strength, including physical soil properties, stress state, solution concentration parameters, and environmental variables such as pH and temperature. More comprehensive reviews can refer to literature [8, 17, 18].

2.1 | Cementation Concentration

The cementation concentration refers to the concentration of urea and calcium chloride, which are the two main injected

ingredients in MICP treatment as described in Equation (1).

$$CO(NH_2)_2 + Ca^{2+} + 2H_2O \xrightarrow{\text{bacteria}} 2NH_4^+ + CaCO_3 \downarrow \quad (1)$$

Extensive studies have been conducted to investigate the effect of cementation concentration on the outcomes of MICP treatment. For instance, Al Qabany and Soga [19] used cementation solution containing equimolar amount of urea and calcium chloride for MICP treatment and found that a higher cementation concentration is more likely to result in precipitation of relatively larger crystals. Xiao et al. [20] utilised microfluidic chips to study the effect of $CaCl_2$ on the homogeneity and quantity of crystal growth. They found that $CaCO_3$ grew faster and distributed more uniformly along the width of the reaction microchannel, given a relatively high $CaCl_2$ concentration. In general, the cementation concentration may affect the size and distribution of the precipitated crystals in the pore space of soil and thus play a role in the strength of bio-cemented soil.

2.2 | Bacterial Strain

The bacterial strain injected into soil produces the urease enzyme, which catalyses urea hydrolysis, while the bacterial cells themselves can serve as nucleation sites for crystal precipitation. Bacterial concentration is typically quantified using optical density at 600 nm wavelength (OD_{600}). Cheng et al. [21] demonstrated that urease activity influences the distribution pattern of the precipitated crystals: $CaCO_3$ is majorly accumulated at the gaps between sand grains for treatment with a low urease activity (1.25 U/mL). By contrast, crystals are more likely to precipitate on the sand grain surface in the case of higher urease activity. They further pointed out that high urease activity increases the saturation for crystal nucleation and growth, facilitating the formation of metastable precursor minerals such as vaterite. Dhami et al. [22] evaluated various bacterial isolates, such as *Bacillus megaterium*, *B. cereus*, *B. thuringiensis* and *B. subtilis* for MICP treatment, finding that different bacterial isolates can produce distinct $CaCO_3$ morphologies. Konstantinou et al. [23] reported that lower urease activity yields more uniformly cemented specimens. Wang et al. [24] found that bacterial density can affect the precipitation rate as well as the number and size of $CaCO_3$ crystals. This evidence indicates that the bacterial strain influences the strength of bio-cemented soil by affecting crystal distribution and morphology.

2.3 | pH

pH is a critical factor in the MICP process, influencing metabolism, urease activity, calcium carbonate crystallisation, and consequently the soil strength [21, 25]. Most urease-producing bacteria used in MICP, such as *Bacillus* and *Sporosarcina*, are well-suited for growth in alkaline environments, with optimal growth typically occurring at pH levels above 9.0 [26]. pH affects microbial cell membrane permeability, which subsequently influences bacterial metabolism. Higher pH environments generally promote faster precipitation rates and yield smaller crystal sizes, while lower pH conditions result in slower precipitation and larger crystals. However, extremely high or low pH environments can inhibit bacterial growth and significantly reduce MICP effectiveness.

2.4 | Temperature

Temperature is another key factor influencing the MICP process. By adjusting temperature, both urease activity and the precipitation rate of $CaCO_3$ can be modified, resulting in varying MICP effectiveness. Based on the temperature dependence of urease activity, Xiao et al. [27] developed a temperature-controlled method and found that uniformity of calcite precipitation can be achieved at approximately 6°C, ensuring the homogeneous distribution of bacteria–reagent mixture solutions in sand specimens. Wang et al. [28] employed microfluidic chip experiments to investigate temperature effects (varying from 4°C–50°C) on MICP process, finding that low temperature (4°C) did not reduce urease activity but limited the final precipitation amount, while also decreasing the bacterial growth and calcium carbonate precipitation rate. By contrast, high temperature (50°C) significantly reduced urease activity. Cheng et al. [29] conducted MICP treatment at three different temperatures (4°C, 25°C and 50°C) and reported that temperature significantly affects both size and distribution of the precipitated crystals in the soil pore space. At a high temperature of 50°C, crystals tend to distribute over the sand grain surface, with a typical size of 2–5 μm. Whereas at 25°C, crystals can be 10 times larger. These larger crystals were found to cover the contact areas of sand grains, which can result in a different mechanical contribution compared to those precipitated at the sand grain surface [30].

2.5 | Soil Properties

The mechanical performance of bio-cemented soil depends not only on the treatment program (e.g., bacterial and cementation concentration, pH and temperature) but also on the intrinsic properties of the soil. While different treatment programs yield varying properties in bio-cemented soils, as discussed previously, different soil types may respond differently to identical treatment protocols. Influential soil properties include particle size, gradation and relative density, as these characteristics determine the pore space controlling bacterial transport. Fine particles such as clay may impede the free flow of bacteria through pore-throats [31]. However, larger particle sizes such as coarse sands may not result in a high mechanical improvement, as soil packings with coarse grains hold less grain contacts, which leads to the majority of crystals coats on the surface of coarse particles rather than the contact points as pointed out by Tang et al. [18], the crystals in this coating pattern may show negligible contribution to the overall strength improvement [30]. Consequently, an optimal particle size range for MICP exists, typically between 50 μm and 10 mm as summarised by Wang and Yin [8], which allows for sufficient bacterial mobility flow through the soil matrix while maintaining enough precipitation sites that can effectively lead to strength improvement.

2.6 | Stress State

It is well established that the soil strength is stress-dependent. While unconfined compressive strength (UCS) provides valuable

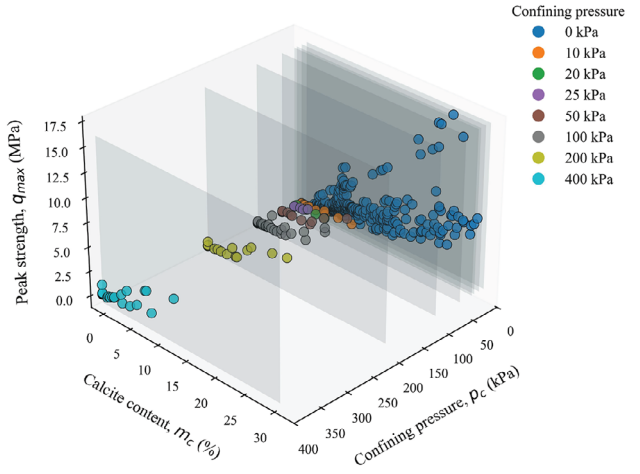

FIGURE 1 | Review of the relationship between peak strength, confining pressure and calcite content. Data from literature [6, 11, 19, 27, 29, 32–49].

baseline measurements, the strength under confined conditions can better represent in situ stress states encountered in geotechnical engineering applications. The soil strength at a certain confining pressure is commonly assessed by the drained triaxial compression test. Xiao et al. [27] conducted a series of drained triaxial compression tests on bio-cemented soils with carbonate content ranging from 0% to approximately 5.1% under confining pressure of 20 to 200 kPa. It was found that given the same carbonate content, the gained strength varies with the confining pressure, while not showing a clear trend. Nafisi et al. [32] conducted drained triaxial compression tests on bio-cemented soils using three different types of sands (Ottawa 2030, Ottawa 5070 and Nevada sands) under 10, 100 and 400 kPa of confining pressure, respectively. Their results indicated that the contribution of cementation to shear strength was more pronounced at a lower effective confining stress. With increasing confining pressure, the enhancement of shear strength became less significant. Such an effect of confining pressure varies across different soil types, highlighting the complex interaction between soil characteristics and stress conditions. These findings demonstrate the important role of confining pressure in determining the strength of bio-cemented soils. A comprehensive review on the strength-confining pressure-calcite content relationship is presented in Figure 1 (data is available in the attachment), highlighting the complex interplay between stress state and calcite content and their joint effect on the resultant soil strength.

3 | Material and Methodology

3.1 | Data Collection and Analysis

The above review suggests that the strength of bio-cemented soil is affected by multiple factors. To compile the dataset, each potential data point collected from the literature is evaluated for completeness across the influencing factors (discussed in Section 2) and the target variable. Wang and Yin [8] compiled a database of 351 samples from literature, considering influencing parameters including the mean grain size D_{50}, coefficient of uniformity C_u, initial void ratio e_0, the optical density at 600 mm wavelength (OD_{600}), urea concentration M_u, calcium concentration M_{Ca} and carbonate content m_c. Nawaz et al. [9] subsequently adopted the same dataset for model training to predict UCS. However, a critical limitation of their dataset is the absence of confining pressure as an input parameter. As mentioned earlier, confining pressure defines the stress state of soil, which significantly affects soil strength and cannot be ignored in practical engineering applications.

To address this limitation, the present study incorporates confining pressure as an additional input parameter, expanding the feature set to eight variables. One hundred nine samples with confining pressures ranging from 20 to 400 kPa are included in the database, with 24 of them being untreated control samples that serve as baseline measurements. These baseline samples enable the model to gain information about the effects of confining pressure on soil strength. While pH and temperature are recognised influencing factors, they are excluded due to the scarcity of reported data for these two factors, which is a common issue also acknowledged by Wang and Yin [8]. The expanded database constructed in this study contains 480 samples [6, 11, 19, 29, 27, 32–49], showing a 37% increase in sample number over the previous dataset. The model information from the literature and this study is summarised and compared in Table 1. It should be noted that potential outliers in the experimental data from the literature are assumed to have been addressed by the original work, as the cited experimental studies typically report only final measured values without providing the error range.

The histogram of the input and output variables is presented in Figure 2. The statistical description of each variable is listed in Table 2, including the minimum, average, maximum and standard deviation values. From Figure 2 and Table 2, it can be seen that the database encompasses soil specimens with substantial variability. The mean grain size ranges from 0.12 mm (fine sand) to 1.6 mm (coarse sand). Most soil specimens in the database are poorly graded ($C_u < 2$), characterised by uniform particle size distribution, though well-graded specimens ($C_u > 6$) with broader particle size ranges are also represented. The initial void ratio indicates that the soil specimens span from loose to dense states, offering insights into different packing densities. The cementation levels (m_c) vary considerably, ranging from lightly cemented specimens to heavily cemented ones, thus enabling analysis across different degrees of cementation.

To quantify the relationship between any two variables, the Pearson correlation coefficient (PCC) is adopted. The results are shown in Figure 3. The proximity of the absolute value of PCC to 1 signifies a greater degree of association between parameters. Notably, there is a strong positive correlation between M_u and M_{Ca}, as solutions containing equimolar urea and $CaCl_2$ are usually used in MICP treatment. The correlation between peak strength (q_{max}) and carbonate content exhibits a strong correlation, suggesting that carbonate content plays a major role in influencing soil strength. The relative importance of each input feature to the output variable can be evaluated by approaches such as permutation importance and Spearman correlation. In this study, Spearman correlation [50] is employed to determine the importance degree of the eight influencing factors. As shown in Figure 4, the carbonate content exhibits the highest importance score, exerting a predominant influence on strength prediction,

TABLE 1 | Summarised models information from the literature and this study.

References	Methods	Dataset	Input variables	Predict variables
Wang and Yin [8]	MEP, MC	351	D_{50}, C_u, e_0, OD_{600}, M_u, M_{Ca}, m_c	UCS
Nawaz et al. [9]	GPR, ANFIS, ANN, GEP	351	D_{50}, C_u, e_0, OD_{600}, M_u, M_{Ca}, m_c	UCS
Sangdeh et al. [10]	ANN-PSO	70	pH, OD_{600}, M_{Ca}, M_u, V_t	m_c
Sangdeh et al. [10]	ANFIS-PSO	115	D_{50}, C_u, e_0, m_c	UCS
This study	BNN	480	D_{50}, C_u, e_0, OD_{600}, M_u, M_{Ca}, m_c, p_c	q_{max}

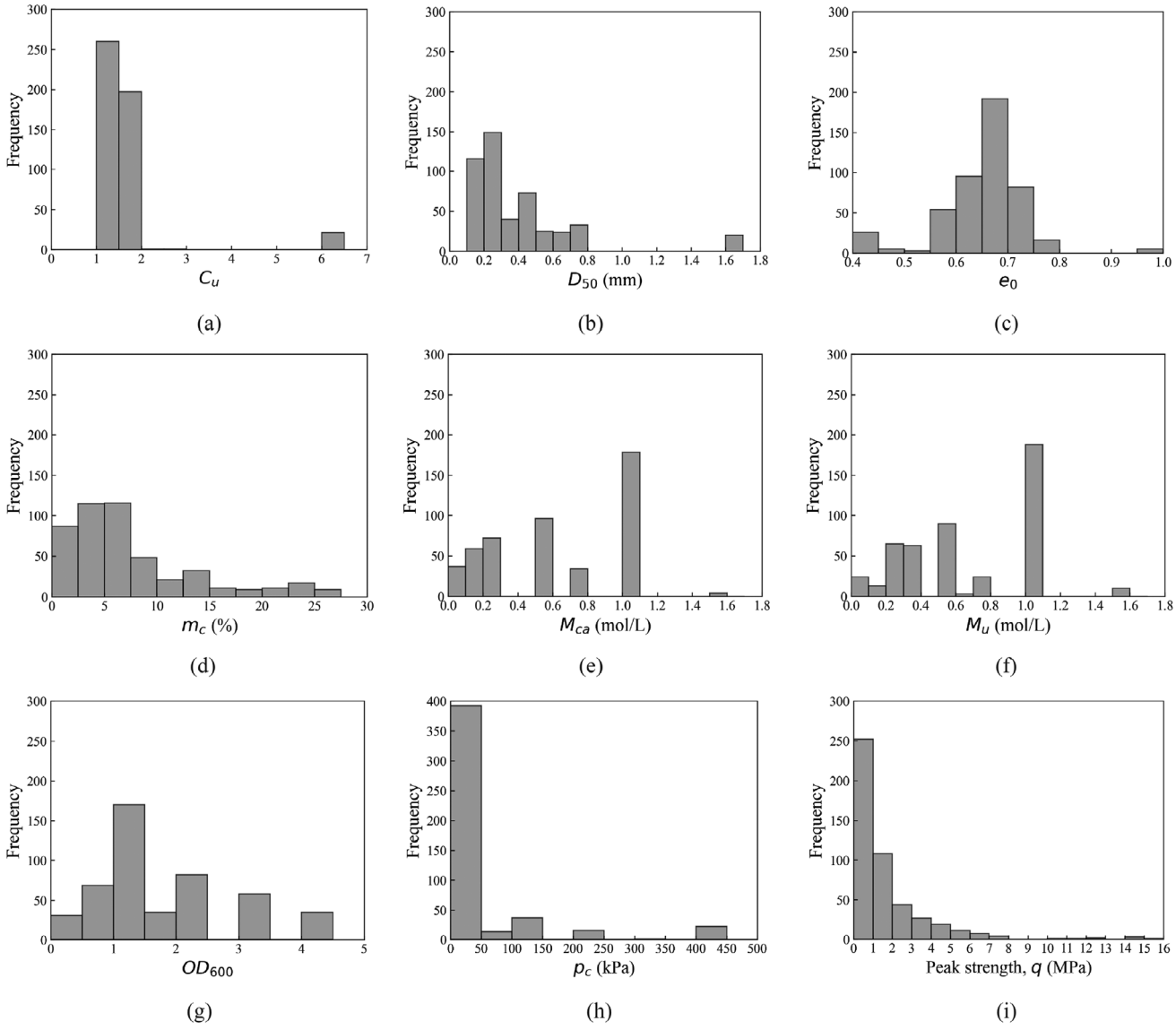

FIGURE 2 | Histogram of input and output variables.

while D_{50} shows the lowest importance. Moreover, p_c ranks as the second most influential parameter, highlighting its critical role for strength prediction. It is worth noting that Pearson correlation measures linear relationships between two variables, while Spearman correlation captures monotonic relationships, which are not necessarily linear. Consequently, p_c shows a weak linear correlation to q_{max} (Figure 3), yet ranks as the second most influential parameter (Figure 4), indicating that p_c has a significant but non-linear effect on soil strength, which is a typical feature of soil behaviour.

3.2 | Data Partitioning and Normalisation

The dataset, consisting of 480 samples, is divided into three subsets: training, validation, and test sets, following

TABLE 2 | Statistical description of input and output variables.

Features	Symbol	Unit	Minimum	Average	Maximum	Std.
Mean grain size	D_{50}	mm	0.12	0.396	1.6	0.307
Coefficient of uniformity	C_u	—	1.17	1.69	6.23	0.990
Initial void ratio	e_0	—	0.41	0.651	1.04	0.083
Optical density	OD_{600}	—	0	1.691	4.46	1.155
Urea concentration	M_u	mol/L	0	0.640	1.5	0.362
Calcium concentration	M_{Ca}	mol/L	0	0.589	1.5	0.380
Carbonate content	m_c	%	0	7.61	29.47	6.55
Confining pressure	p_c	kPa	0	34.95	400	91.75
Peak deviatoric stress	q_{max}	MPa	0.018	1.67	15.96	2.15

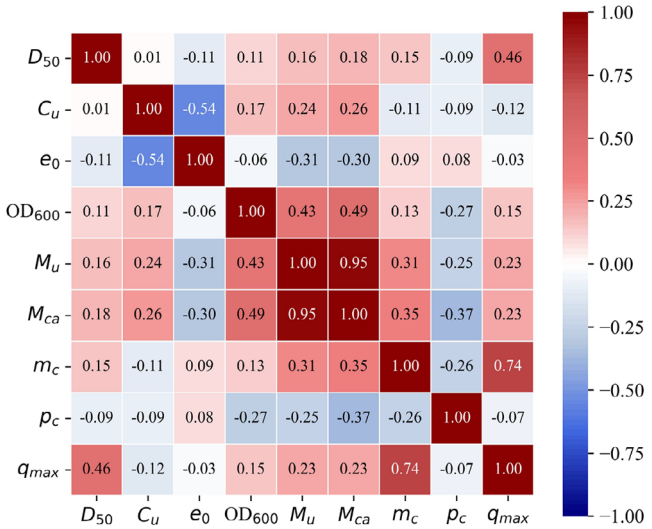

FIGURE 3 | Heatmap of Pearson correlation coefficient.

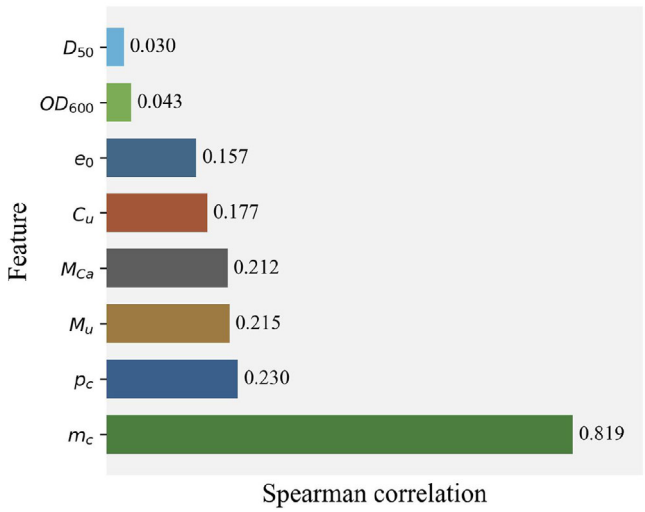

FIGURE 4 | Importance degree of 8 influencing factors using Spearman correlation.

a 70%:15%:15% ratio. The training set (70% of data) is used to optimise model parameters, and the validation set (15% of data) guides hyperparameter selection. The test set (15% of data) remains unused during the training and validation processes, serving as an independent benchmark for final model evaluation.

To facilitate the training of models for bio-cemented soil strength, a systematic data partitioning approach is adopted. *Z*-score standardisation is employed in this study to convert the input features to a common scale [51]. In this way, the effects of features with different magnitudes can be mitigated and the convergence efficiency during the optimisation process can be enhanced. *Z*-score standardisation transforms each feature to have a zero mean and unit variance. For a given feature vector $\mathbf{X}$, the standardised value $\mathbf{X}'$ is calculated as:

$$\mathbf{X}' = \frac{\mathbf{X} - \mu}{\sigma} \tag{2}$$

where μ represents the mean of the feature vector and σ denotes its standard deviation.

3.3 | Artificial Neural Network (ANN)

A typical ANN architecture includes an input layer, one or more hidden layers and an output layer [52], as illustrated in Figure 5a. Each layer consists of one or multiple neurons. The number of input and output neurons corresponds to the number of input features and the variables to be predicted, respectively. The number of hidden layers and neurons in each of the hidden layers is the hyperparameters that need to be tuned to achieve a good performance. Note that the values (e.g., 0.3, 0.6, etc.) in Figure 5a represent deterministic weights in a conventional ANN, where each connection has a deterministic weight parameter. These specific values are arbitrary examples chosen for illustration purposes.

For the feedforward calculation, the output of each neuron can be expressed as:

$$z_i^l = \sum_{j=1}^{n^{l-1}} w_{ij}^l a_j^{l-1} + b_i^l \tag{3}$$

$$a_i^l = f(z_i^l) \tag{4}$$

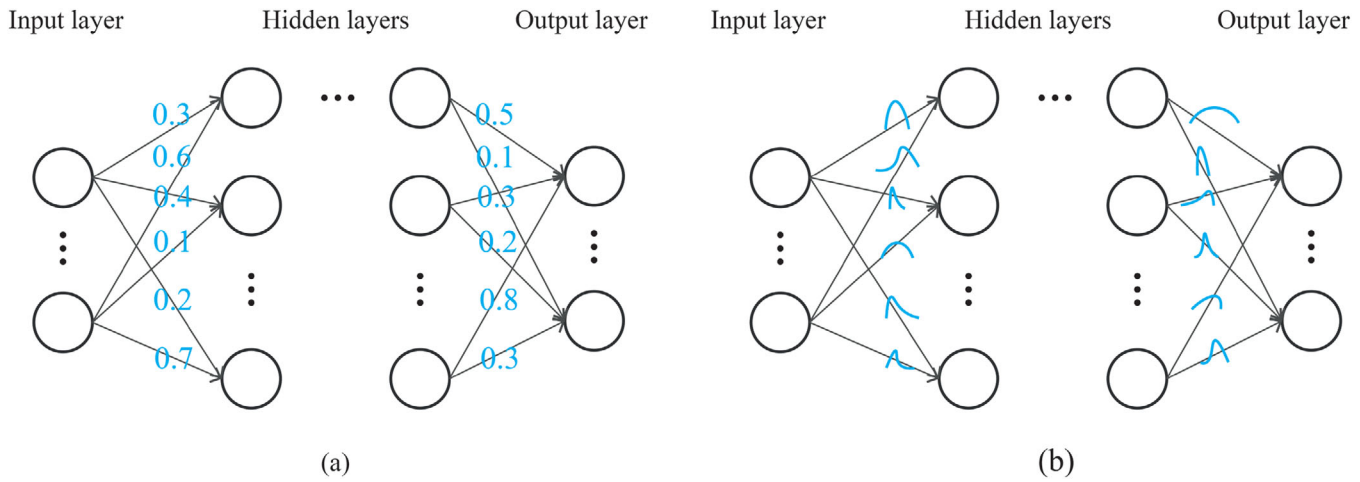

FIGURE 5 | Illustration of the conceptual architecture of (a) artificial neural network; (b) Bayesian neural network. The specific values and curves are arbitrary examples chosen for illustration purposes.

where l represents the layer number and n^l represents the number of neurons in layer l. z_i^l is the weighted input to the ith neuron in layer l, w_{ij}^l is the weight connecting the jth neuron in layer $(l-1)$ to the ith neuron in layer l, a_j^l is the activation of the jth neuron in layer l, b_i^l is the bias and f is the activation function. In this study, Rectified Linear Unit (ReLU) is used as the activation function.

The weight and bias are updated through the backpropagation process, specifically:

$$w_{ij}^l \leftarrow w_{ij}^l - \eta \frac{\partial L}{\partial w_{ij}^l} \tag{5}$$

$$b_i^l \leftarrow b_i^l - \eta \frac{\partial L}{\partial b_i^l} \tag{6}$$

where η is the learning rate and is taken as 0.01 in the study (determined by trial-and-error). L is the loss function, which is the mean square error (MSE) in this study (see Section 3.6). The loss function is optimised using the gradient-based Adam optimiser [53].

3.4 | Bayesian Neural Network (BNN)

A Bayesian neural network (BNN) is one type of ANN that applies Bayesian inference to quantify uncertainty in its predictions, generating probabilistic outputs instead of deterministic ones [54]. As illustrated in Figure 5, the weights and biases in ANN are deterministic parameters, while they are represented by a probability distribution (e.g., Gaussian) in BNN. During training, these distributions are updated using Bayes' theorem to obtain posterior distributions, as follows:

$$p(y|x,D) = \int p(y|x,\theta)p(\theta|D)d\theta \tag{7}$$

$$p(\theta|D) = \frac{p(D|\theta)p(\theta)}{p(D)} \tag{8}$$

where $p(\theta)$ is the prior distribution of weights and biases, $p(D|\theta)$ is the likelihood of the data given the weights and biases, and $p(D)$ is the evidence.

3.5 | Variational Inference in Bayesian Neural Networks

In Bayesian Neural Networks (BNNs), we aim to learn a distribution over the model's parameters (weights and biases) rather than fixed point estimates. This allows the model to capture epistemic uncertainty and make probabilistic predictions. The core goal is to compute the posterior distribution $p(\theta|D)$. However, this posterior is generally intractable for neural networks due to the high-dimensional, nonlinear nature of the parameter space. Variational Inference (VI) [55] provides an efficient alternative by introducing a family of simpler, tractable distributions $q(\theta)$, known as the variational distribution, to approximate the true posterior.

Rather than sampling from $p(\theta|D)$, VI frames inference as an optimisation problem [56]: it minimises the Kullback–Leibler (KL) divergence between $q(\theta)$ and $p(\theta|D)$. Since the true posterior is unknown, this is done indirectly by maximising the Evidence Lower Bound (ELBO):

$$\text{ELBO} = \mathbb{E}_{q(\theta)}[\log p(D|\theta)] - \text{KL}(q(\theta)\|p(\theta)) \tag{9}$$

The first term is the expected log-likelihood, which encourages the model to fit the data, while the second term penalises divergence from the prior, which acts as a regulariser.

The variational parameters, such as the mean and standard deviation of each parameter's approximate posterior, are optimised by stochastic gradient descent. To make predictions, we draw multiple samples from the approximate posterior $q(\theta)$ and pass them through the model. The resulting distribution over predictions provides both the mean estimate and uncertainty.

3.6 | Model Performance Criteria

Three statistical indicators are used to evaluate the performance in this study: mean square error (MSE), root mean square error (RMSE) and coefficient of determination (R^2). They are defined as below:

$$\mathrm{MSE} = \frac{1}{N}\sum_{i=1}^{N}(y_i - \hat{y}_i)^2 \tag{10}$$

$$\mathrm{RMSE} = \left[\frac{1}{N}\sum_{i=1}^{N}(y_i - \hat{y}_i)^2\right]^{\frac{1}{2}} \tag{11}$$

$$R^2 = 1 - \frac{\sum_{i=1}^{N}(y_i - \hat{y}_i)^2}{\sum_{i=1}^{N}(y_i - \bar{y})^2} \tag{12}$$

where N is the number of samples, y_i is the actual value, $\hat{y}_i$ is the predicted value, and $\bar{y}$ is the mean of actual values. The MSE measures the average of the squares of the errors. RMSE is the square root of MSE, which brings the error metric back to the same scale as the original data. The R^2 value ranges from 0 to 1, indicating the proportion of variance in the dependent variable that is predictable from the independent variables, with 1 representing perfect prediction. These metrics are selected for model performance evaluation as RMSE (or MSE) quantifies the magnitude of prediction errors between predicted and true soil strength values. R^2 assesses how effectively the model accounts for the variability in soil strength compared to its mean. These indicators are widely used for assessing predictive model performance for soil properties.

3.7 | Activation Function

The rectified linear unit (ReLU) is adopted as the activation function for both ANN and BNN in this study, as it is widely used in neural networks due to its fast convergence rate and effectiveness in mitigating the vanishing gradient problem [13, 57]. It is defined as:

$$\mathrm{ReLU}(x) = \max(0, x) \tag{13}$$

where x is the input to the activation function. The ReLU function outputs x for positive inputs and zero for negative inputs, making it computationally efficient and sparsely activated.

4 | Results

4.1 | Evaluation of ANN Model

As listed in Table 2, eight variables, namely, D_{50}, C_u, e_0, OD_{600}, M_u, M_{Ca}, m_c and p_c, are used as the input features of the ANN, and thus the number of neurons of the input layer of the ANN is eight. The output layer has a single neuron that corresponds to the peak strength (q_{max}). A trial-and-error process is adopted to find the optimal depth (the number of hidden layers) and width (the number of neurons in each hidden layer). In this process, ANNs with various combinations of depth and width are built and evaluated in which depth ∈ [1,6] and width ∈ [6,64]. The performances are compared in Table 3.

TABLE 3 | RMSE of ANNs with different depth and width.

Width	Depth					
	1	2	3	4	5	6
6	0.764	0.702	0.889	0.832	0.649	0.966
12	0.699	0.608	0.700	0.788	0.830	0.646
18	0.662	0.693	0.740	0.637	0.695	0.628
32	0.791	0.770	0.601	0.726	**0.557**	0.591
64	0.734	0.774	0.732	0.804	0.696	0.668

Note: The bold value (lowest RMSE) indicates the optimal width and depth for the ANN.

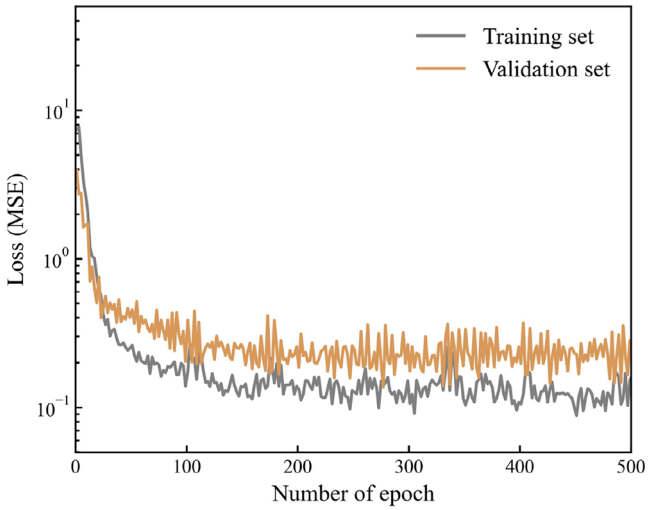

FIGURE 6 | The learning curve based on MSE for the ANN model.

According to Table 3, the optimal artificial neural network architecture was determined to be a depth of 5 with a width of 32, achieving performance metrics of RMSE = 0.557, MSE = 0.31 and R^2 = 0.923. In comparison, Nawaz et al. [9], developed an ANN model for predicting UCS of bio-cemented soils using the 351 data points constructed by Wang and Yin [8], achieving a performance of R^2 = 0.941 and RMSE = 0.512. While the ANN model developed in this study exhibits a slightly lower R^2, it is essential to recognise that the R value by itself does not offer a complete evaluation of a model's predictive accuracy [58, 59]. The comparable RMSE values between the two models suggest equivalent performance, which is particularly noteworthy given that the present model incorporates stress condition as an additional parameter, which may increase model complexity.

Figure 6 presents the evolution of loss values for the training and validation sets of the ANN model with the selected configuration (depth of 5 and width of 32). It can be seen that the model converges fast and reaches a stable level. The comparable performance metrics between training and validation datasets suggest that the trained model demonstrates a consistent level of accuracy and good generalisation capability. The comparison between predicted values and true values, as well as the error distribution of the ANN model, is presented in Figure 7, which displays characteristics consistent with a near-normal distribu-

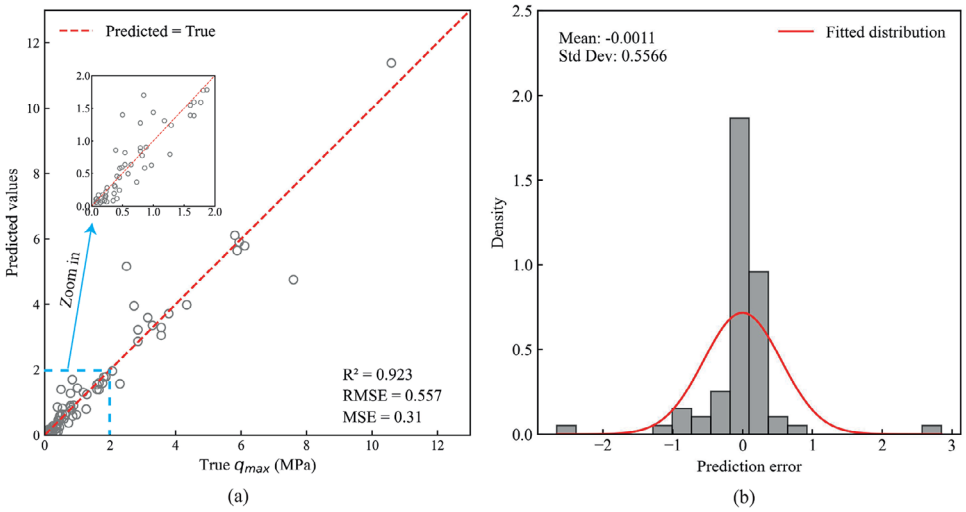

FIGURE 7 | (a) Comparison between true q_{max} and the predicted value; (b) error distribution of the ANN model.

tion, centred close to zero with a mean of -0.0011 and standard deviation of 0.5566.

4.2 | Evaluation of BNN Model

The BNN model is developed using a trial-and-error process. A systematic approach is employed for hyperparameter optimisation. Bayesian optimisation, implemented using Optuna, is employed to explore the hyperparameter space, with hidden layer 1 size ∈ [32, 128], hidden layer 2 size ∈ [16, 64], and learning rate ∈ [1e-5, 1e-3]. The optimisation objective is to minimise the validation loss over 5000 training epochs. Based on this exploration, the final architecture of BNN comprises 128 and 64 neurons in the first and second hidden layers, respectively, with a learning rate of 5e-5. The BNN employs normal distribution priors ($\mu = 0, \sigma = 1$) for all weights and biases, with posterior distributions approximated using Variational Inference (VI) and the Adam optimiser to minimise the loss function. The use of normal priors for weights and biases is very common in Bayesian neural networks, due to their ability to promote stable convergence. While alternative priors such as the Laplace distribution can induce sparsity, they may impose overly restrictive weight flexibility, potentially leading to convergence difficulties.

For uncertainty quantification, the BNN leverages posterior predictive sampling to generate comprehensive probability distributions for each prediction, from which a 95% credible interval is derived to characterise prediction confidence bounds.

Figure 8 presents the evolution of ELBO for both the training and validation sets for BNN. The epoch for training is set to 30,000 for the training of BNN. It can be seen from Figure 8 that this epoch is large enough to reach a convergent status. Figure 9 shows the distribution of true values against predicted means across all test samples, with the associated uncertainty represented by the 95% credible interval. It can be seen that the predicted means closely track the true values. The probabilistic framework quantifies prediction uncertainty through a 95% credible interval, with narrower bounds in data-dense regions and expanded intervals where data is sparse, suggesting a good predictive performance

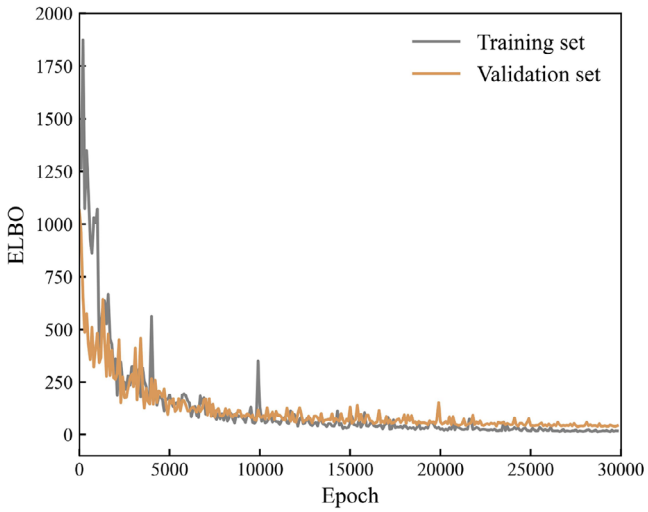

FIGURE 8 | The learning curve of the BNN model.

of the developed BNN model. It should be noted that the model shows more accurate predictive capacity for low strength specimens (e.g., $q_{max} < 2$ MPa), as most true values in these ranges fall within the 95% credible interval. By contrast, several specimens show larger prediction errors for q_{max} around 2 to 6 MPa.

The comparison between the predicted mean value and the true q_{max} with 95% error bar is shown in Figure 10a, from which the uncertainty is quantified. It further demonstrates that the uncertainty is larger for q_{max} ranging above 2 MPa than for low values. This suggests that bio-cemented soils with higher strength would exhibit greater uncertainty in prediction. This increased uncertainty for high-strength samples may be attributed to both limited training data and inherent physical variability (discussed in Section 5). Future experimental studies focusing on high-strength bio-cemented soil samples are therefore recommended to better analyse these uncertainty sources. The present BNN model achieves performance metrics of RMSE = 0.768, MSE = 0.589 and $R^2 = 0.853$. Compared to the developed deterministic ANN model ($R^2 = 0.923$, RMSE = 0.557), the BNN exhibits

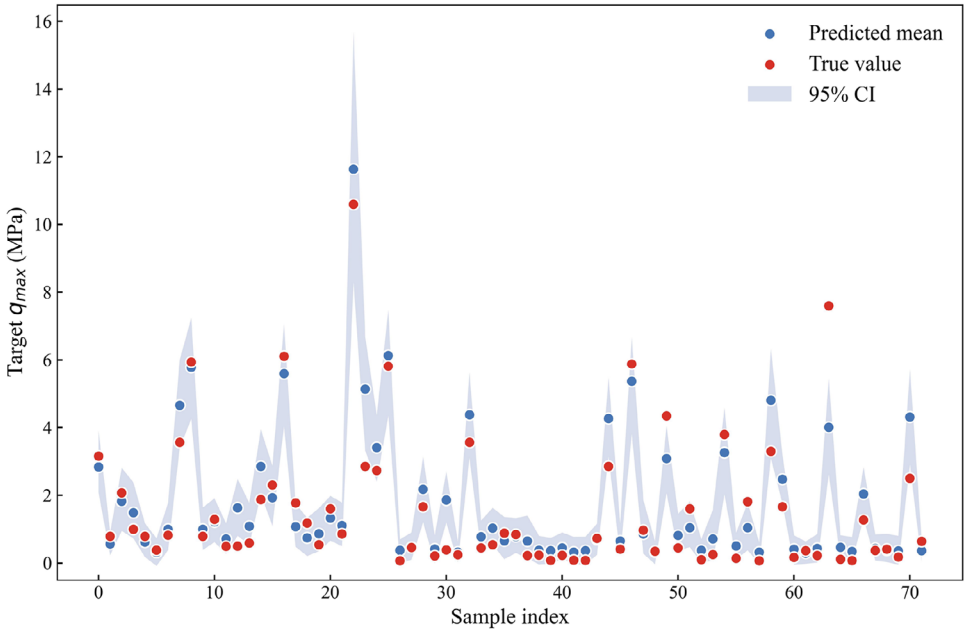

FIGURE 9 | The predicted mean, 95% credible interval (CI), along with the true value for the BNN model.

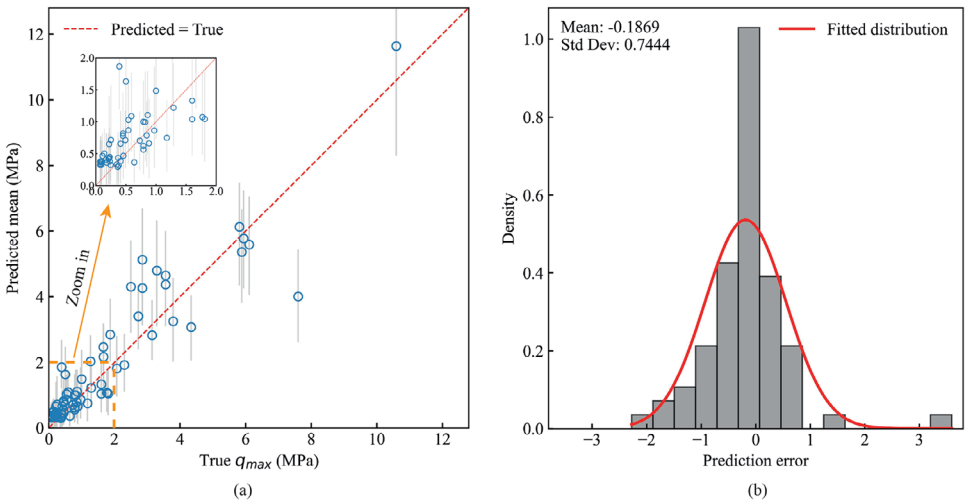

FIGURE 10 | (a) Comparison between true q_{max} and the predicted mean value; (b) error distribution of the BNN model.

slightly lower prediction accuracy in terms of point estimates. It is important to note that BNN does not necessarily provide better predictive performance than conventional ANN; rather, its primary advantage lies in the incorporation of uncertainty quantification. The error distribution of the BNN model is plotted in Figure 10b, which can be described by a normal distribution with a mean error of −0.187 and a standard deviation of 0.744. Compared to the error distribution of the ANN model shown in Figure 7, the mean error of both models is negligibly small relative to the measurement scale, though the BNN model presents a higher standard deviation.

To interpret the uncertainty of BNN predictions across the range of each input parameter. Figure 11 and Figure 12 correlate the predicted q_{max} with each input feature for the training and validation set, along with a 95% credible interval (CI) using BNN. It should be noted that in this way the plots do not indicate the relationship between q_{max} and each input parameter, as the values of the remaining parameters are different at each data point.

Two regions can be identified in Figure 11 and Figure 12: a dense data region, where most data points fall within, and a sparse data region where fewer data points are present. The 95% credible interval bands in dense data regions are generally narrow, suggesting less uncertainty and high confidence. Specifically, the uncertainty increases substantially when D_{50} exceeds 0.7 mm. For C_u and p_c, uncertainty remains consistently low across their respective ranges. The model demonstrates low uncertainty for e_0 between 0.55 and 0.78. When OD_{600} exceeds 3, uncertainty increases markedly. Both M_u and M_{Ca} show increasing uncertainty at higher concentrations, with M_{Ca} exhibiting larger uncertainty above 0.5 mol/L. Most notably, higher m_c generally corresponds to increased uncertainty, particularly above 10%. The

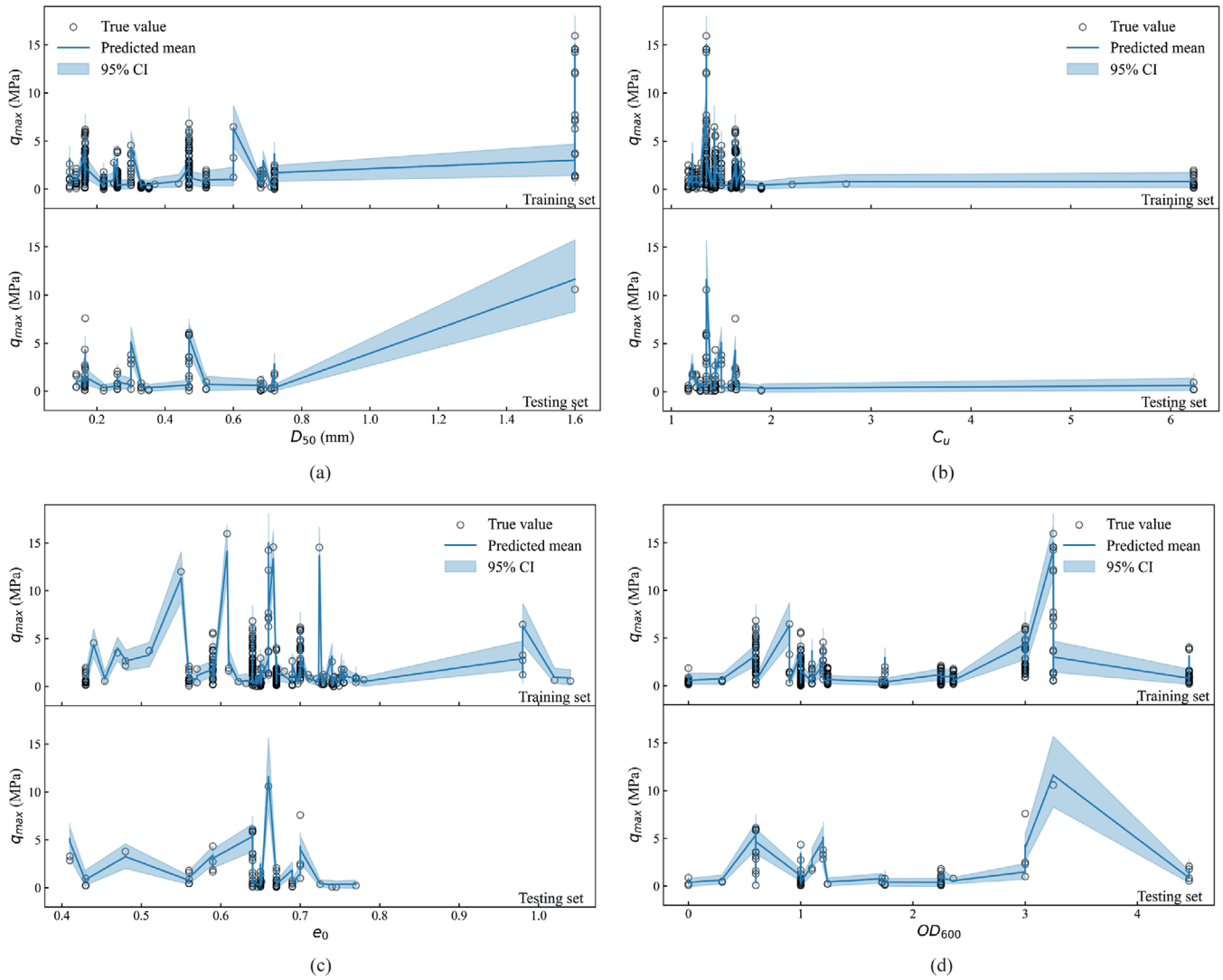

FIGURE 11 | Correlations between predicted q_{max} and input features for training and testing set: (a) D_{50}, (b) C_u, (c) e_0 and (d) OD_{600}.

potential physical mechanisms leading to the uncertainty are discussed in Section 5.

5 | Discussion on Physics Leading to Uncertainty

While the developed BNN model enables the prediction of bio-cemented soil strength and the quantification of prediction uncertainty, understanding the underlying physical mechanisms causing this uncertainty is essential for improving future predictive models. BNN predictions reveal that even with identical input features (e.g., the eight features adopted in this study), the predicted strength can exhibit notable variation. This uncertainty reflects the complex nature of the bio-cementation process and cannot be attributed solely to model limitations. Rather, it emerges from fundamental physical mechanisms across different scales. To understand the physics that may lead to the uncertainty, in this section, the uncertainty in bio-cemented soil strength is discussed from two scales: the particle scale and the soil element scale, respectively. At the particle scale, variation in crystal precipitation pattern and contact properties introduces randomness to the strengthening process. Meanwhile, at the soil element scale, heterogeneity can be induced due to the bacterial transport mechanisms and chemical diffusion processes in the soil pore space. Overall, these physical processes, which can not be fully considered in the input features in the BNN model, contribute to variability and uncertainty in bio-cemented soil strength. The detailed discussion is provided as follows.

5.1 | Distribution Pattern of Precipitated Crystals

Grain-scale observations on bio-cemented soils using scanning electron microscopy (SEM) and micro-CT revealed that the crystals can precipitate in different patterns within the pore space of soils. As illustrated in Figure 13, crystals may precipitate at grain contacts (contact cementing), at gaps between sand grains forming as a bridge (bridging), coat the sand grain (coating), filling in the void space and not bonding to sand grains (pore filling), and connect to multiple sand grains forming a matrix (matrix supporting) [12, 30, 60].

The mechanical contribution of each precipitation pattern varies substantially. Zhang and Dieudonné [30] and Zhang et al.

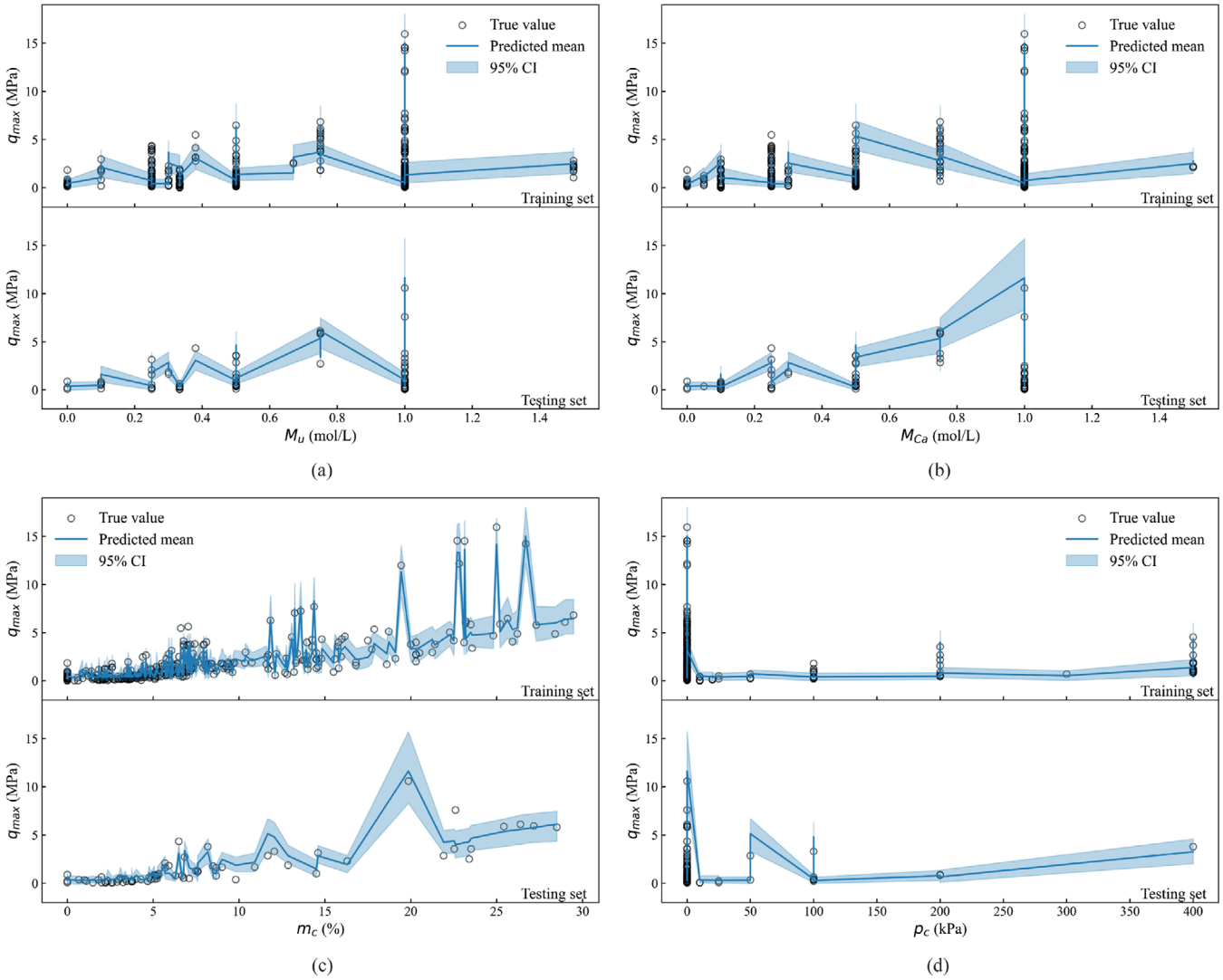

FIGURE 12 | Correlations between predicted q_{max} and input features for training and testing set: (a) M_u, (b) M_{Ca}, (c) m_c and (d) p_c.

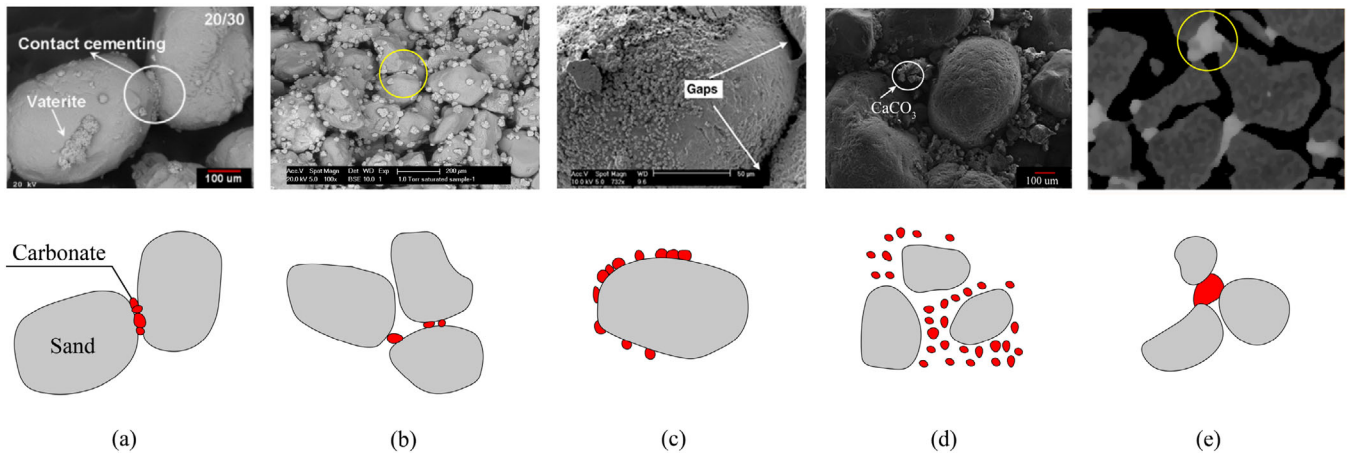

FIGURE 13 | Experimental observation [12, 25, 36, 49, 61] and conceptualisation [30] of bio-cemented soils at the grain scale for different crystal distribution patterns: (a) contact cementing; (b) bridging; (c) coating; (d) pore filling; (e) matrix supporting.

[62] used the discrete element method to explicitly model bio-cemented specimens with ideal carbonate distribution patterns. The results demonstrated that even with identical carbonate content (m_c), the contact cementing and bridging patterns generated significantly greater improvements in both strength and stiffness compared to coating and pore-filling patterns. Although crystal distribution patterns can be influenced by factors such as cementation solution composition and temperature (see Section 2), these microscale precipitation characteristics cannot be fully described by the macroscale input features used in the BNN model. This limitation introduces an inherent source of uncertainty in strength predictions, as the same set of input parameters may result in different microscale crystal arrangements and consequently variable mechanical properties.

5.2 | Crystal Morphology and Shape

Besides distribution patterns, the morphology and shape of calcium carbonate crystals also contribute significantly to uncertainty in bio-cemented soil strength. During MICP treatment, $CaCO_3$ can precipitate in any of $CaCO_3$ polymorphs: vaterite, aragonite and calcite. Additionally, metastable hydrated forms can develop, including monohydrocalcite ($CaCO_3 \cdot H_2O$), ikaite ($CaCO_3 \cdot 6H_2O$), calcium carbonate hemihydrate ($CaCO_3 \cdot 1/2H_2O$), and amorphous calcium carbonate (ACC) [25, 63, 64]. Each of these crystal forms possesses distinct mechanical properties. For instance, the Young's modulus ranges from as low as 25 GPa for ACC [65] to 96.8 GPa for calcite [66, 67]. In the DEM model of bio-cemented sands in Zhang et al. [62], the stiffness of precipitated crystals was varied to represent different crystal morphologies. Their results demonstrated that higher crystal stiffness leads to greater small-strain stiffness as well as peak strength, providing support that the variation in crystal morphology significantly influences the overall mechanical behaviour of bio-cemented soils and contributes to the observed variability in strength outcomes.

Various shapes of precipitated crystals have been observed from bio-cemented soils, including rhombohedral-shaped crystals, cubic plate-like crystals and spherical crystals [11, 25, 42]. Crystal shape is intrinsically linked to its polymorphic structure. Vaterite, aragonite and calcite typically exhibit hexagonal, orthorhombic and rhombohedral structures, respectively [63]. Although the effect of crystal shape on the mechanical improvement of bio-cemented soil remains underexplored in current literature to the best of the authors' knowledge, analogous research on soil particle shape demonstrated the importance of particle shape on soil mechanical behaviour [68]. The irregular geometries generally increase inter-particle rolling resistance and, consequently, overall strength. This suggests that the variation in crystal shape introduces uncertainty in strength prediction, as they cannot be directly represented by the macroscale input parameters used in the predictive models.

5.3 | Spatial Heterogeneity

Beyond the particle-scale variations as discussed above, spatial heterogeneity at the soil element scale introduces another significant dimension of uncertainty in bio-cemented soil strength. Experimental data from Terzis et al. [69], plotted in Figure 14, clearly demonstrate the non-uniform distribution of $CaCO_3$ mass. In general, higher concentrations of $CaCO_3$ mass are observed at the top or bottom compared to the middle portion of specimens. This phenomenon has also been reported by Xiao et al. [70], who found that $CaCO_3$ tends to precipitate in the upper part of the specimen using a room-temperature two-phase MICP method[1]. In contrast, one-phase treatment methods[2], such as the one-phase low-pH injection method proposed by Cheng et al. [21] and the temperature-controlled one-phase MICP method established by Xiao et al. [70], have demonstrated improved capacity to achieve more uniform biocement distribution throughout soil specimens.

The impact of $CaCO_3$ heterogeneity on bio-cemented soil strength has been evaluated through both experimental and numerical investigations. In experimental studies, Xiao et al. [70] demonstrated that specimens with relatively uniform $CaCO_3$ distribution achieved higher peak strength compared to heterogeneous specimens with equivalent carbonate content. These findings were further supported by numerical simulations conducted by Zhang and Dieudonné [71] using discrete element modelling. Their study examined bio-cemented specimens with varying degrees of $CaCO_3$ heterogeneity subjected to drained triaxial compression testing. The results revealed a significant influence of spatial distribution uniformity on mechanical performance. Specifically, specimens with heterogeneous $CaCO_3$ distribution exhibited strength improvement ratios $(q_{max}^{cemented} - q_{max}^{uncemented})/q_{max}^{uncemented}$, up to 12% lower than specimens with uniform cementation, despite containing identical total carbonate content. This combined experimental and numerical evidence confirms that spatial heterogeneity not only exists in bio-cemented soils but also substantially impacts their strength, thereby introducing an additional source of uncertainty.

5.4 | Predominant Orientation of Calcite Bond

Soil fabric characterises the arrangement and orientation of particles, particle contacts and pore spaces. It represents a fundamental aspect of granular materials that significantly influences their mechanical behaviour [72, 73]. Advanced microscopic investigations have revealed variations in fabric characteristics among bio-cemented specimens. Terzis and Laloui [12] evaluated fabric characteristics of bio-cemented soils in the 3D space via micro-CT. Their findings demonstrated that calcite bonds in medium-grained sand exhibit relatively homogeneous distribution in the theta-orientation space. In contrast, calcite bonds formed in fine-grained sand showed anisotropic characteristics, with predominant orientations at approximately 45° and 235°.

Despite the experimental evidence showing that the calcite bonds can present different predominant orientations. The link between the orientation of calcite bonds and strength variation remains unclear, as it is difficult to fabricate bio-cemented samples with designed calcite orientations in laboratory experiments, whereas DEM allows precise control of the microstructure and has been successfully applied in previous studies on bio-cemented soils [30, 74]. To this end, this section presents a supplementary DEM investigation, aiming at investigating how calcite bonds with different predominant orientations potentially affect bio-cemented soil strength.

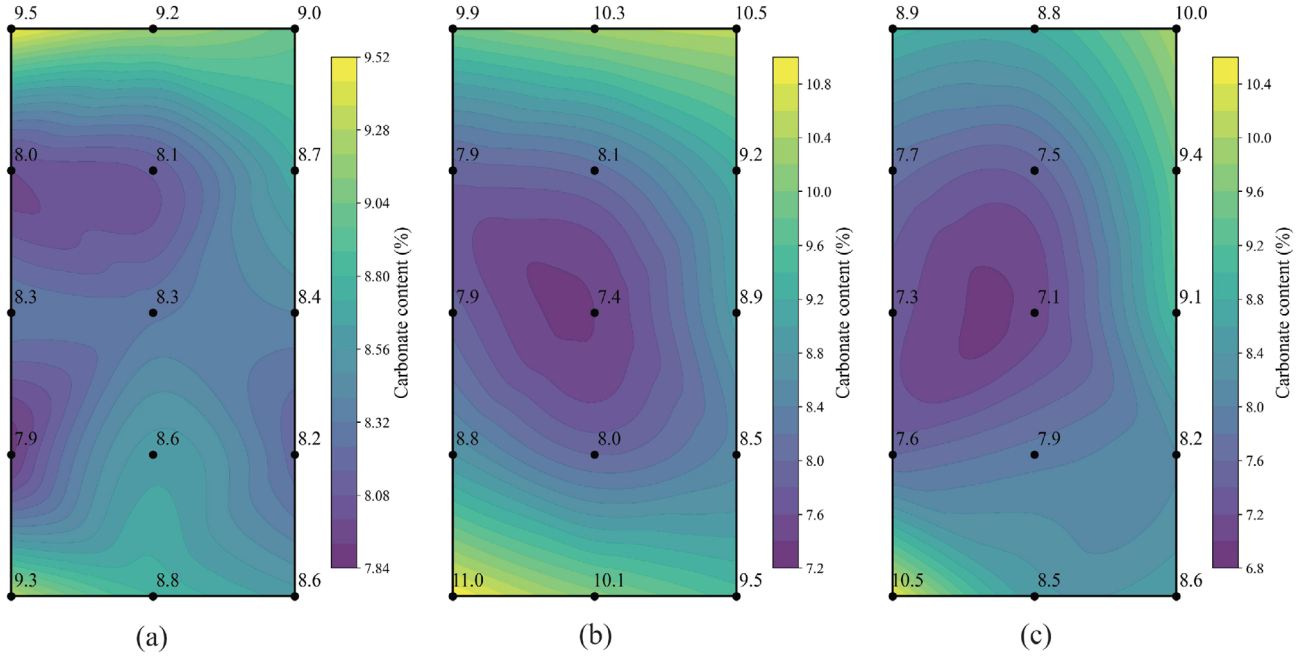

FIGURE 14 | Distribution of the precipitated $CaCO_3$ mass within a bio-cemented specimen. Data from Terzis et al. [69].

The DEM simulation conducted in this study is based on YADE [75]. The presented model is quasi-2D. It consists of 10,000 spherical particles confined within a 1 m × 2 m domain bounded by four rigid walls. The 2D condition is simulated by placing the centres of all spheres on the same plane and blocking the translation and rotations in the out-of-plane direction. Particle radii are uniformly distributed between 5.5 mm and 8.3 mm, with a mean radius of 6.9 mm. The initial void ratio of the DEM packing is 0.26, defined in 2D as the ratio of void area to solid area in the plane of particle centers.

A cohesive-frictional contact model [75] is employed. This contact model incorporates rolling and twisting resistance to account for irregular particle shape effect. In the uncemented specimen, all inter-particle contacts are purely frictional. In the cemented specimen, the cementation effect is simulated by incorporating inter-particle cohesion. Note that cohesion is applied only to contacts with orientations falling within the specified directional range, other contacts remain frictional. For the sake of simplicity, the contact model is not described in this study; its details can be found in YADE [75] and Zhang and Dieudonné [30]. The parameters used in the DEM simulations are summarised in Table 4.

Two bonding configurations are examined, as illustrated in Figure 15. In Case A, all the inter-particle contacts whose direction (i.e. contact normal vector) is located in range of 0° ± 45° (relative to the horizontal axis) are cemented by assigning a cohesive force in the normal and shear direction, note that the opposite direction (180° ± 45°) is also included; In Case B, the same cohesive forces are applied, but only to contacts whose directional vectors fall within the range of 90° ± 45° or 270° ± 45°. Consequently, the two specimens have distinct bond orientations, which can be seen from Figure 16. It is important to note that the number of contacts satisfying the directional criterion in Case A is 8205, which differs from the 7847 contacts for Case B. Assuming that the number of cemented contacts represents the amount of cementation, 7847 contacts are randomly selected from the 8205 contacts to ensure an equivalent amount of cementation in both cases.

TABLE 4 | Properties of particles used in the DEM simulations.

Properties	Symbol	Unit	Value
Density	ρ	kg/m^3	2650
Young's modulus	E	MPa	200
Shearing stiffness coefficient	ν	—	0.3
Friction angle	φ_c'	°	20
Rolling stiffness coefficient	α_r	—	0.4
Twisting stiffness coefficient	α_{tw}	—	0.4
Rolling resistance coefficient	η_r	—	0.4
Twisting resistance coefficient	η_{tw}	—	0.4
Normal adhesion	σ_n	N	500
Shear adhesion	σ_s	N	500

The two specimens are subjected to drained biaxial compression tests. The stress-strain relationship is compared in Figure 17. It can be seen that the predominant orientation of the bond significantly affects the mechanical behaviour. The peak strength of Case A is 1.4 times that of Case B. This finding supports that the variation in cementation fabric contributes to the uncertainty of soil strength. When $CaCO_3$ bonds exhibit preferential orientations, the specimen develops anisotropic strength that varies with loading direction. This directional dependency suggests that specimens with identical $CaCO_3$ content may display significantly different strength responses depending on the loading orientation relative to their internal fabric.

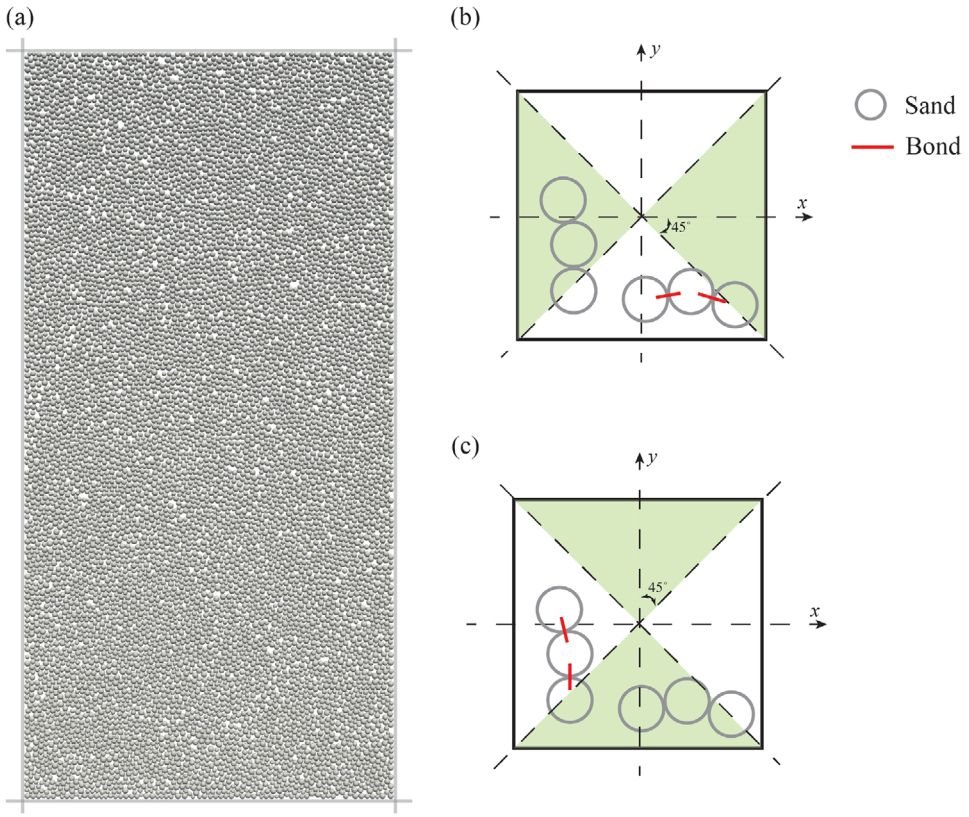

FIGURE 15 | Illustration of (a) the DEM specimen, and schematics of selected contacts with predominant orientation: (b) range of 0° ± 45° and (c) 90° ± 45°. The opposite direction is also considered.

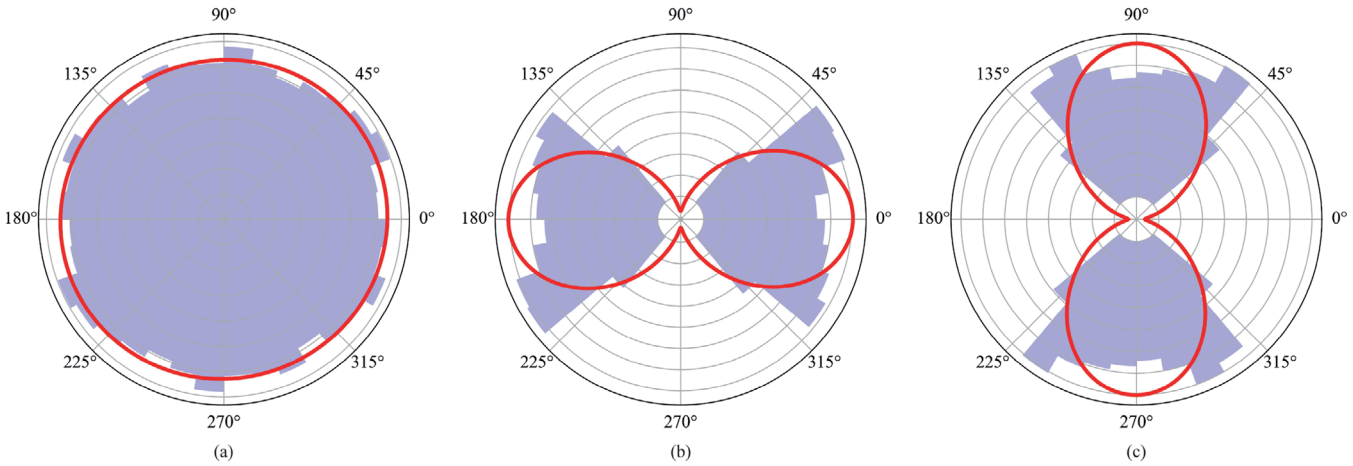

FIGURE 16 | Rose diagram (with fitted curve in red) showing the contact normal distribution: (a) all inter-particle contacts of uncemented specimen; (b) bonded contacts in Case A; (c) bonded contacts in Case B.

6 | Conclusions

Predicting the strength of bio-cemented soil is challenging due to the complex bio-chemo-hydro-mechanical multiphysics processes involved. This study leverages artificial intelligence to address this challenge by developing a Bayesian neural network model that can effectively predict bio-cemented soil strength from multiple influencing factors while quantifying prediction uncertainty. Several key contributions are made in this study:

- A more comprehensive database containing 480 experimental samples has been constructed by expanding upon a published database, representing a 37% increase in data compared to the former dataset.
- The confining pressure has been incorporated as an input feature for strength prediction, thereby enabling a more realistic representation of in situ stress states encountered in geotechnical applications.

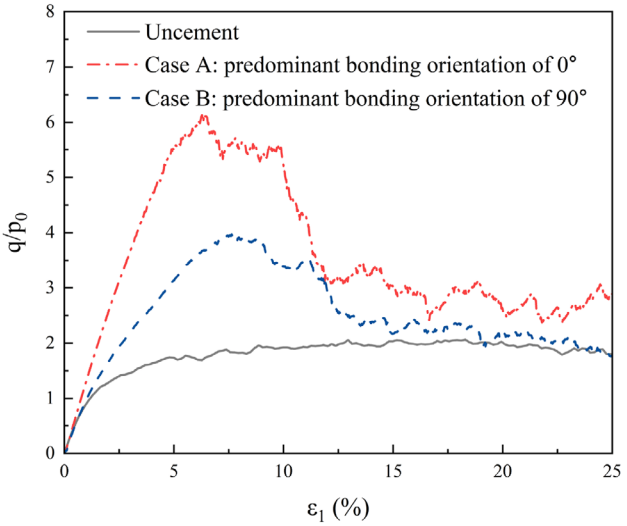

FIGURE 17 | Comparison of stress-strain relationship between DEM cemented specimens with different bond orientations: Case A for predominant bonding orientation of 0°. q is the deviatoric stress, p_0 is the confining pressure, ε_1 is the axial strain.

- The prediction uncertainty is quantified using the BNN model, providing confidence intervals that reflect the varying degrees of predictive reliability across different strength ranges.
- A comprehensive discussion of physical mechanisms underlying strength prediction uncertainty is presented, supported by DEM simulations conducted in this study and existing DEM studies from the literature.

Feature-specific analysis revealed that carbonate content and confining pressure are the most influential parameters affecting bio-cemented soil strength, confirming the importance of including confining pressure in strength prediction. Both ANN and BNN models demonstrate effective predictive capabilities, with the BNN model providing additional quantification of uncertainty. This consideration of uncertainty is essential for predicting bio-cemented soil strength, as the strength is affected by multiscale factors that can not be fully described by the input features of predictive models.

Four sources of strength variability are discussed across scales. Their links to strength uncertainty are supported by DEM simulations conducted in this study and the literature. At the particle scale, variations in crystal distribution pattern, morphology, shape and fabric contribute to strength variability. At the soil element scale, spatial heterogeneity in $CaCO_3$ mass distribution introduces additional dimensions of uncertainty that cannot be captured by the input features.

The developed BNN model can be a valuable alternative for predicting bio-cemented soil strength with quantified reliability and supports the design of MICP treatments. For a given soil condition and a specified target strength, the model can be used to determine the optimal treatment parameters, such as urea and calcium concentrations. In addition, the BNN provides uncertainty quantification, which supports risk assessment. Conditions identified with high uncertainty indicate potential risks and may require enhanced monitoring or alternative treatment strategies. This capability promotes the implementation of MICP in geotechnical applications.

While this study provides valuable insights, certain limitations could be improved in future research. The input parameters, though carefully selected based on physical significance, may not capture all factors influencing bio-cemented soil behaviour, such as pH, temperature, and detailed microstructural characteristics, due to insufficient experimental data. Future research can incorporate additional input parameters, particularly those related to microstructural characteristics, as micro-CT and image analysis techniques become more accessible. In addition, it is recommended to develop multi-output BNN models capable of simultaneously predicting strength and stiffness, which would provide more comprehensive design tools for practical applications.

Author Contributions

Aoxi Zhang: data curation, methodology, analysis, writing – original draft, review and editing. **Liang Wang:** methodology, analysis, writing – original draft. **Wengang Zhang:** review and editing. **Chaofa Zhao:** review and editing, funding acquisition. **Pan Zhang:** analysis, review and editing.

Acknowledgments

The following funds are greatly acknowledged for the support: National Natural Science Foundation of China (Grant No. 52311530699), National Key Research and Development Program of China (No. 2023YFB2604200), Key R&D Program of Zhejiang Province (No. 2023C03182), and Zhejiang Provincial Natural Science Foundation of China (No. LQ23E080013).

Conflicts of Interest

The authors declare no conflicts of interest.

Data Availability Statement

The data that support the findings of this study are available on request from the corresponding author. The data are not publicly available due to privacy or ethical restrictions.

Endnotes

[1]The two-phase method means that bacterial solution is injected into the soil in the first phase and retained for a certain time for the transportation of bacteria, then followed by injecting cementation solution in the second phase [42, 76].

[2]Bacterial and cementation solutions are injected as a mixture.

References

1. J. DeJong, K. Soga, E. Kavazanjian, et al., "Biogeochemical Processes and Geotechnical Applications: Progress, Opportunities and Challenges," *Géotechnique* 63, no. 4 (2013): 287–301.

2. J. He, J. Chu, Y. Gao, and H. Liu, "Research Advances and Challenges in Biogeotechnologies," *Geotechnical Research* 6, no. 2 (2019): 144–155.

3. S. Zhang, S. Wang, Z. Ahmed, and X. Zhao, "A Novel Mathematical Model for Repairing Rough Cracks Using the Microbially Induced Carbonate Precipitation (MICP)," *Sustainability* 15, no. 17 (2023): 13122.

4. S. Zhang, S. Wang, Z. Ahmed, and F. Alshawmar, "Application of Microbially Induced CaCO3 on the Reinforcement of Rock Discontinuity," *Applied Sciences* 14, no. 19 (2024): 8952.

5. X. Deng, Z. Wang, Y. Qin, et al., "Experimental Study on the Reinforcement of Calcareous Sand Using Combined Microbial-Induced Carbonate Precipitation (MICP) and Festuca Arundinacea Techniques," *Journal of Marine Science and Engineering* 13, no. 5 (2025): 883.

6. L. Cheng, R. Cord-Ruwisch, and M. A. Shahin, "Cementation of Sand Soil by Microbially Induced Calcite Precipitation at Various Degrees of Saturation," *Canadian Geotechnical Journal* 50, no. 1 (2013): 81–90.

7. X. Gai and M. Sánchez, "An Elastoplastic Mechanical Constitutive Model for Microbially Mediated Cemented Soils," *Acta Geotechnica* 14, no. 3 (2019): 709–726.

8. H. L. Wang and Z. Y. Yin, "Unconfined Compressive Strength of bio-Cemented Sand: State-of-the-Art Review and MEP-MC-Based Model Development," *Journal of Cleaner Production* 315 (2021): 128205.

9. M. N. Nawaz, A. Y. Akhtar, W. Hassan, M. H. A. Khan, and M. M. Nawaz, "Artificial Intelligence-Based Prediction Models of Bio-Treated Sand Strength for Sustainable and Green Infrastructure Applications," *Transportation Geotechnics* 46 (2024): 101262.

10. M. K. Sangdeh, M. Salimi, H. H. Khansar, et al., "Predicting the Precipitated Calcium Carbonate and Unconfined Compressive Strength of bio-Mediated Sands Through Robust Hybrid Optimization Algorithms," *Transportation Geotechnics* 46 (2024): 101235.

11. D. Mujah, L. Cheng, and M. A. Shahin, "Microstructural and Geomechanical Study on Biocemented Sand for Optimization of MICP Process," *Journal of Materials in Civil Engineering* 31, no. 4 (2019): 04019025.

12. D. Terzis and L. Laloui, "Cell-Free Soil Bio-Cementation With Strength, Dilatancy and Fabric Characterization," *Acta Geotechnica* 14, no. 3 (2019): 639–656.

13. P. Zhang, Z. Y. Yin, and Y. F. Jin, "Bayesian Neural Network-Based Uncertainty Modelling: Application to Soil Compressibility and Undrained Shear Strength Prediction," *Canadian Geotechnical Journal* 59, no. 4 (2022): 546–557.

14. X. Gu, L. Wang, Q. Ou, W. Zhang, and G. Sun, "Reliability Assessment of Rainfall-Induced Slope Stability Using Chebyshev–Galerkin–KL Expansion and Bayesian Approach," *Canadian Geotechnical Journal* 60, no. 12 (2023): 1909–1922.

15. L. Han, W. Zhang, L. Wang, J. Fu, L. Xu, and Y. Wang, "A Reliability Analysis Framework Coupled With Statistical Uncertainty Characterization for Geotechnical Engineering," *Geoscience Frontiers* 15, no. 6 (2024): 101913.

16. W. Zhang, S. Liu, L. Wang, et al., "The Overall Stability of a Partially Unstable Reservoir Bank Slope to Water Fluctuation and Rainfall Based on Bayesian Theory," *Landslides* 21, no. 8 (2024): 2021–2032.

17. J. T. DeJong, B. M. Mortensen, B. C. Martinez, and D. C. Nelson, "Bio-Mediated Soil Improvement," *Ecological Engineering* 36, no. 2 (2010): 197–210.

18. C. S. Tang, L. Y. Yin, N. J. Jiang, et al., "Factors Affecting the Performance of Microbial-Induced Carbonate Precipitation (MICP) Treated Soil: A Review," *Environmental Earth Sciences* 79, no. 5 (2020): 1–23.

19. A. Al Qabany and K. Soga, "Effect of Chemical Treatment Used in MICP on Engineering Properties of Cemented Soils," *Géotechnique* 63, no. 4 (2013): 331–339.

20. Y. Xiao, X. He, A. W. Stuedlein, J. Chu, T. M. Evans, and L. A. van Paassen, "Crystal Growth of MICP Through Microfluidic Chip Tests," *Journal of Geotechnical and Geoenvironmental Engineering* 148, no. 5 (2022): 06022002, https://doi.org/10.1061/(ASCE)GT.1943-5606.0002756.

21. L. Cheng, M. A. Shahin, and J. Chu, "Soil Bio-Cementation Using a New One-Phase Low-pH Injection Method," *Acta Geotechnica* 14, no. 3 (2019): 615–626.

22. N. K. Dhami, M. S. Reddy, and A. Mukherjee, "Biomineralization of Calcium Carbonate Polymorphs by the Bacterial Strains Isolated From Calcareous Sites," *Journal of Microbiology and Biotechnology* 23, no. 5 (2013): 707–714.

23. C. Konstantinou, Y. Wang, G. Biscontin, and K. Soga, "The Role of Bacterial Urease Activity on the Uniformity of Carbonate Precipitation Profiles of Bio-Treated Coarse Sand Specimens," *Scientific Reports* 11, no. 1 (2021): 1–17.

24. Y. Wang, K. Soga, J. T. DeJong, and A. J. Kabla, "Effects of Bacterial Density on Growth Rate and Characteristics of Microbial-Induced CaCO3 Precipitates: Particle-Scale Experimental Study," *Journal of Geotechnical and Geoenvironmental Engineering* 147, no. 6 (2021): 04021036.

25. L. A. Van Paassen, *Biogrout, Ground Improvement by Microbial Induced Carbonate Precipitation* (PhD thesis, Delft University of Technology, 2009).

26. G. D. Okwadha and J. Li, "Optimum Conditions for Microbial Carbonate Precipitation," *Chemosphere* 81, no. 9 (2010): 1143–1148.

27. Y. Xiao, Y. Wang, C. Desai, X. Jiang, and H. Liu, "Strength and Deformation Responses of Biocemented Sands Using a Temperature-Controlled Method," *International Journal of Geomechanics* 19, no. 11 (2019): 04019120.

28. Y. Wang, Y. Wang, K. Soga, J. T. DeJong, and A. J. Kabla, "Microscale Investigations of Temperature-Dependent Microbially Induced Carbonate Precipitation (MICP) in the Temperature Range 4–50°C," *Acta Geotechnica* (2022): 1–23.

29. L. Cheng, M. A. Shahin, and D. Mujah, "Influence of key Environmental Conditions on Microbially Induced Cementation for Soil Stabilization," *Journal of Geotechnical and Geoenvironmental Engineering* 143, no. 1 (2017): 04016083.

30. A. Zhang and A. C. Dieudonné, "Effects of Carbonate Distribution Pattern on the Mechanical Behaviour of bio-Cemented Sands: A DEM Study," *Computers and Geotechnics* 154 (2023): 105152.

31. J. K. Mitchell and J. C. Santamarina, "Biological Considerations in Geotechnical Engineering," *Journal of Geotechnical and Geoenvironmental Engineering* 131, no. 10 (2005): 1222–1233.

32. A. Nafisi, B. M. Montoya, and T. M. Evans, "Shear Strength Envelopes of Biocemented Sands With Varying Particle Size and Cementation Level," *Journal of Geotechnical and Geoenvironmental Engineering* 146, no. 3 (2020): 04020002.

33. L. A. van Paassen, R. Ghose, T. van der Linden, W. van der Star, and M. C. M. van Loosdrecht, "Quantifying Biomediated Ground Improvement by Ureolysis: Large-Scale Biogrout Experiment," *Journal of Geotechnical and Geoenvironmental Engineering* 136, no. 12 (2010): 1721–1728.

34. L. Cheng, M. Shahin, and R. Cord-Ruwisch, "Bio-Cementation of Sandy Soil Using Microbially Induced Carbonate Precipitation for Marine Environments," *Géotechnique* 64, no. 12 (2014): 1010–1013.

35. Q. Zhao, L. Li, C. Li, M. Li, F. Amini, and H. Zhang, "Factors Affecting Improvement of Engineering Properties of MICP-Treated Soil Catalyzed by Bacteria and Urease," *Journal of Materials in Civil Engineering* 26, no. 12 (2014): 04014094.

36. H. Lin, M. T. Suleiman, D. G. Brown, and E. Kavazanjian Jr, "Mechanical Behavior of Sands Treated by Microbially Induced Carbonate Precipitation," *Journal of Geotechnical and Geoenvironmental Engineering* 142, no. 2 (2015): 04015066.

37. B. Montoya and J. DeJong, "Stress-Strain Behavior of Sands Cemented by Microbially Induced Calcite Precipitation," *Journal of Geotechnical and Geoenvironmental Engineering* 141, no. 6 (2015): 04015019.

38. K. Feng and B. Montoya, "Influence of Confinement and Cementation Level on the Behavior of Microbial-Induced Calcite Precipitated Sands Under Monotonic Drained Loading," *Journal of Geotechnical and Geoenvironmental Engineering* 142, no. 1 (2016): 04015057.

39. A. Mahawish, A. Bouazza, and W. P. Gates, "Effect of Particle Size Distribution on the bio-Cementation of Coarse Aggregates," *Acta Geotechnica* 13 (2018): 1019–1025.

40. A. Mahawish, A. Bouazza, and W. P. Gates, "Improvement of Coarse Sand Engineering Properties by Microbially Induced Calcite Precipitation," *Geomicrobiology Journal* 35, no. 10 (2018): 887–897.

41. A. Mahawish, A. Bouazza, and W. P. Gates, "Unconfined Compressive Strength and Visualization of the Microstructure of Coarse Sand Subjected to Different Biocementation Levels," *Journal of Geotechnical and Geoenvironmental Engineering* 145, no. 8 (2019): 04019033.

42. A. Nafisi, S. Safavizadeh, and B. M. Montoya, "Influence of Microbe and Enzyme-Induced Treatments on Cemented Sand Shear Response," *Journal of Geotechnical and Geoenvironmental Engineering* 145, no. 9 (2019): 06019008.

43. K. Wen, Y. Li, S. Liu, C. Bu, and L. Li, "Development of an Improved Immersing Method to Enhance Microbial Induced Calcite Precipitation Treated Sandy Soil Through Multiple Treatments in low Cementation Media Concentration," *Geotechnical and Geological Engineering* 37 (2019): 1015–1027.

44. Y. Xiao, X. He, T. M. Evans, A. W. Stuedlein, and H. Liu, "Unconfined Compressive and Splitting Tensile Strength of Basalt Fiber–Reinforced Biocemented Sand," *Journal of Geotechnical and Geoenvironmental Engineering* 145, no. 9 (2019): 04019048.

45. I. Ahenkorah, M. Rahman, M. Karim, and P. Teasdale, "A Comparison of Mechanical Responses for Microbial-and Enzyme-Induced Cemented Sand," *Géotechnique Letters* 10, no. 4 (2020): 559–567.

46. T. Hoang, J. Alleman, B. Cetin, and S. G. Choi, "Engineering Properties of Biocementation Coarse-and Fine-Grained Sand Catalyzed by Bacterial Cells and Bacterial Enzyme," *Journal of Materials in Civil Engineering* 32, no. 4 (2020): 04020030.

47. A. Nafisi, D. Mocelin, B. M. Montoya, and S. Underwood, "Tensile Strength of Sands Treated With Microbially Induced Carbonate Precipitation," *Canadian Geotechnical Journal* 57, no. 10 (2020): 1611–1616.

48. Y. Wang, C. Konstantinou, K. Soga, J. T. DeJong, G. Biscontin, and A. J. Kabla, "Enhancing Strength of MICP-Treated Sandy Soils: From Micro to Macro Scale," *arXiv preprint arXiv:2006.15760* (2020).

49. S. Wu, B. Li, and J. Chu, "Stress-Dilatancy Behavior of MICP-Treated Sand," *International Journal of Geomechanics* 21, no. 3 (2021): 04020264.

50. C. Spearman, "The Proof and Measurement of Association Between two Things," *American Journal of Psychology* 100, no. 3/4 (1987): 441–471.

51. J. Zhang, Y. Zhu, X. Zhang, M. Ye, and J. Yang, "Developing a Long Short-Term Memory (LSTM) Based Model for Predicting Water Table Depth in Agricultural Areas," *Journal of Hydrology* 561 (2018): 918–929.

52. Y. LeCun, Y. Bengio, and G. Hinton, "Deep Learning," *Nature* 521, no. 7553 (2015): 436–444.

53. D. P. Kingma, "Adam: A Method for Stochastic Optimization," *arXiv preprint arXiv:1412.6980* (2017).

54. M. S. Khan and P. Coulibaly, "Bayesian Neural Network for Rainfall-Runoff Modeling," *Water Resources Research* 42, no. 7 (2006).

55. D. M. Blei, A. Kucukelbir, and J. D. McAuliffe, "Variational Inference: A Review for Statisticians," *Journal of the American statistical Association* 112, no. 518 (2017): 859–877.

56. A. Graves, "Practical Variational Inference for Neural Networks," in *Advances in Neural Information Processing Systems* (ACM, 2011), 2348–2356.

57. I. Goodfellow, Y. Bengio, A. Courville, and Y. Bengio, *Deep Learning* (MIT Press Cambridge, 2016).

58. H. Güllü, "Function Finding via Genetic Expression Programming for Strength and Elastic Properties of Clay Treated With Bottom Ash," *Engineering Applications of Artificial Intelligence* 35 (2014): 143–157.

59. J. Li, "Assessing the Accuracy of Predictive Models for Numerical Data: Not r nor r2, why not? Then What?," *PloS one* 12, no. 8 (2017): e0183250.

60. H. Lin, M. T. Suleiman, D. G. Brown, and E. Kavazanjian Jr, "Mechanical Behavior of Sands Treated by Microbially Induced Carbonate Precipitation," *Journal of Geotechnical and Geoenvironmental Engineering* 142, no. 2 (2016): 04015066.

61. L. Cheng, M. A. Shahin, and D. Mujah, "Influence of key Environmental Conditions on Microbially Induced Cementation for Soil Stabilization," *Journal of Geotechnical and Geoenvironmental Engineering* 143, no. 1 (2016): 04016083.

62. A. Zhang, V. Magnanimo, H. Cheng, T. J. Heimovaara, and A. C. Dieudonné, "DEM Investigation Into the Small-Strain Stiffness of bio-Cemented Soils," *Acta Geotechnica* (2024): 1–15.

63. A. Clarà Saracho, S. K. Haigh, T. Hata, et al., "Characterisation of CaCO3 Phases During Strain-Specific Ureolytic Precipitation," *Scientific Reports* 10, no. 1 (2020): 1–12.

64. A. C. Saracho, L. Lucherini, M. Hirsch, et al., "Controlling the Calcium Carbonate Microstructure of Engineered Living Building Materials," *Journal of Materials Chemistry A* 9, no. 43 (2021): 24438–24451.

65. S. W. Lee, Y. J. Kim, Y. H. Lee, H. Guim, and S. M. Han, "Behavior and Characteristics of Amorphous Calcium Carbonate and Calcite Using CaCO3 Film Synthesis," *Materials & Design* 112 (2016): 367–373.

66. G. Chahi, D. Bradai, and I. Belabbas, "Structural and Elastic Properties of CaCO3 Hydrated Phases: A Dispersion-Corrected Density Functional Theory Study," *Journal of Physics and Chemistry of Solids* 138 (2020): 109295.

67. J. Ekprasert, I. Fongkaew, P. Chainakun, R. Kamngam, and W. Boonsuan, "Investigating Mechanical Properties and Biocement Application of CaCO3 Precipitated by a Newly-Isolated *Lysinibacillus* sp. WH Using Artificial Neural Networks," *Scientific Reports* 10, no. 1 (2020): 1–13.

68. R. Kawamoto, E. Andò, G. Viggiani, and J. E. Andrade, "All You Need Is Shape: Predicting Shear Banding in Sand With LS-DEM," *Journal of the Mechanics and Physics of Solids* 111 (2018): 375–392.

69. D. Terzis and R. Bernier-Latmani, and L. Laloui, "Fabric Characteristics and Mechanical Response of Bio-Improved Sand to Various Treatment Conditions," *Géotechnique Letters* 6, no. 1 (2016): 50–57.

70. Y. Xiao, Y. Wang, S. Wang, et al., "Homogeneity and Mechanical Behaviors of Sands Improved by a Temperature-Controlled One-Phase MICP Method," *Acta Geotechnica* 16, no. 5 (2021): 1417–1427.

71. A. Zhang and A. C. Dieudonné, *Effects of Carbonate Distribution Inhomogeneity on the Improvement Level of Bio-Cemented Sands: A DEM Study* (Springer, 2023), 554–561.

72. C. F. Zhao and N. P. Kruyt, "An Evolution law for Fabric Anisotropy and its Application in Micromechanical Modelling of Granular Materials," *International Journal of Solids and Structures* 196 (2020): 53–66.

73. C. F. Zhao, G. Pinzón, M. Wiebicke, E. Andò, N. P. Kruyt, and G. Viggiani, "Evolution of Fabric Anisotropy of Granular Soils: X-ray Tomography Measurements and Theoretical Modelling," *Computers and Geotechnics* 133 (2021): 104046.

74. J. Shen, H. Wang, B. Zhou, G. Hu, X. Zhang, and B. Yang, "Investigation of the Effect of Microbial-Induced Calcite Precipitation Treatment on bio-Cemented Calcareous Sands Using Discrete Element Method," *Computers and Geotechnics* 158 (2023): 105365.

75. V. Šmilauer, et al., *Yade Documentation* (The Yade Project, 2021), http://yade-dem.org/doc/.

76. V. S. Whiffin, L. A. Van Paassen, and M. P. Harkes, "Microbial Carbonate Precipitation as a Soil Improvement Technique," *Geomicrobiology Journal* 24, no. 5 (2007): 417–423.